

Article

Characteristics of Large-Scale Coherent Structures on Irregularly Arranged Rough-Bed Open-Channel Flows

Yongqiang Wang ¹, Peng Zhang ^{2,*}, Shengfa Yang ², Chunhong Hu ³, Jianling Jin ¹ and Rangang Zhang ¹

¹ School of River & Ocean Engineering, Chongqing Jiaotong University, Chongqing 400074, China

² National Engineering Research Center of Inland Waterway Regulation, Chongqing Jiaotong University, Chongqing 400074, China

³ State Key Laboratory of Simulation and Regulation of Water Cycle in River Basin, China Institute of Water Resources and Hydropower Research, Beijing 100048, China

* Correspondence: zhangpenghh@cqjtu.edu.cn

Abstract: Large-scale coherent structures (LSCSs) in rough-bed open-channel flow (OCF) are significant in turbulence research. A recent breakthrough is the bimodal feature of LSCSs on regular rough-bed OCF (i.e., LSCSs exhibit two typical motions: large-scale motions (LSMs) and very-large-scale motions (VLSMs)). However, the presence and characteristics of LSMs and VLSMs in irregularly arranged rough-bed OCF remain unclear. Thus, in this study, high-precision indoor flume experiments were performed under typical irregularly arranged rough-bed conditions, and time-resolved particle image velocimetry was used for velocity measurements. Statistical quantities of velocity fluctuations revealed that the friction Reynolds number and roughness exerted a certain modulation on the velocity fluctuating properties. The spectra of velocity fluctuations provided direct and statistical evidence for the presence of LSMs and VLSMs in irregularly arranged rough-bed OCF. VLSMs contributed more than 60% of the streamwise turbulent kinetic energy and 40% of the Reynolds shear stress in the outer region of the irregularly arranged rough-bed OCF, which was slightly higher than that in the smooth-bed or regular rough-bed OCF scenarios. No apparent dependence of the wavelength of VLSMs on the flow submergence (H/d_{50}) was observed in the present irregularly arranged rough-bed OCF, which is in contrast to that reported for regular rough-bed OCF. Furthermore, the relationship between the peak wavelength of VLSMs and the aspect ratio did not strictly follow a linear increase, in contrast to that documented in the literature.



Citation: Wang, Y.; Zhang, P.; Yang, S.; Hu, C.; Jin, J.; Zhang, R.

Characteristics of Large-Scale Coherent Structures on Irregularly Arranged Rough-Bed Open-Channel Flows. *Water* **2023**, *15*, 1105.

<https://doi.org/10.3390/w15061105>

Academic Editors: Giuseppe Oliveto and Giuseppe Pezzinga

Received: 1 February 2023

Revised: 2 March 2023

Accepted: 9 March 2023

Published: 14 March 2023



Copyright: © 2023 by the authors. Licensee MDPI, Basel, Switzerland. This article is an open access article distributed under the terms and conditions of the Creative Commons Attribution (CC BY) license (<https://creativecommons.org/licenses/by/4.0/>).

1. Introduction

Wall-bounded turbulent flows with smooth or rough walls/beds are ubiquitous in nature and engineering applications and have attracted increasing interest in the turbulence research community. Since the 1960s, it has been recognized that wide scales of coherent structures (or motions and eddies) are present in wall-bounded turbulent flows. The scales of these structures range from the viscous length scale $l_* = \nu/u_\tau$ (ν is the kinetic viscosity, and u_τ is the friction velocity) to the outer length scale δ_0 (δ_0 can be the boundary layer thickness in the turbulent boundary layer, the pipe radius in pipe flow, the channel half-height in closed channel flow, and the water depth in open-channel flow (OCF)). Compared to small-scale coherent structures, which have been well characterized, large-scale coherent structures (LSCSs) at scales of the order of δ_0 have been less understood for a long time because of their inherent complexities and capturable and visualizable difficulties both in experiments and simulations.

One of the most important findings regarding the LSCSs over the past two decades is the discovery of their bimodal features (i.e., the LSCSs exhibit two types of motion, large-scale motion (LSM) and very-large-scale motion (VLSM)). LSMs and VLSMs were first documented by Kim and Adrian [1] (1999) in PF from the observation of two peaks

at streamwise wavelengths of the order of pipe radii R and $10R$ (corresponding to LSMs and VLSMs, respectively) in the pre-multiplied spectra of streamwise velocity fluctuations. Although the origin of VLSMs remains unclear and under debate [2], the presence and characteristics of VLSMs have been identified in various wall turbulence scenarios, such as pipe flow [3–5], closed channel flow [6–8], the turbulent boundary layer [9–12], and the atmospheric surface layer [13–15]. The differences observed in the characteristics of VLSMs in different flow scenarios [16–20] indicate that boundary conditions play an important role in shaping the characteristics of VLSMs.

Investigations of VLSMs in OCF have emerged later than those of motions in other flows. To the best of our knowledge, the first study on VLSMs in OCF was conducted by Cameron et al., in 2017 [21]. Based on long-duration particle image velocimetry (PIV) measurements and pre-multiplied spectrum analysis, Cameron et al. provided the first experimental evidence of the presence of VLSMs in regular rough-bed OCF. Since then, investigations of VLSMs in OCF have received increased attention, and the presence and characteristics of VLSMs in various OCF scenarios, such as smooth-bed uniform OCF [22–24], smooth-bed decelerating OCF [25], smooth-bed narrow OCF [26], smooth-bed and particle-laden OCF [27], highly rough-bed OCF [28], regular rough-bed OCF covered with one movable sphere [29], and rough-bed OCF with streamwise ridges [18], have been investigated in recent years. Many unique characteristics of VLSMs in OCF compared to those in other wall flows have been revealed (e.g., the presence of VLSMs extends further away from the wall, accompanied by stronger strength in OCF and occurs at a much lower Reynolds number than that of the other wall flows), indicating the significant influence of the unique upper boundary condition of the free surface in OCF on VLSMs. The effects of turbulence coherent structures on the start and sustainment of sediment transport [30], the energy contribution of coherent structures in OCF to the entrainment of sediment particles, and the rearrangement of river bed surfaces [31] have also been well studied.

Although significant progress has been made in the research on VLSMs in OCF, relevant studies are still limited, and many problems must be clarified. One of the limitations of previous studies is that they were confined to simple bed conditions, such as a smooth-bed [32,33] or a regular rough-bed [34,35]. However, irregularly arranged rough-beds are more common in nature and require further investigation. Furthermore, although the VLSMs in rough-bed OCF (or more precisely, regular rough-bed OCF) have been preliminary investigated, some conclusions are still controversial and difficult to interpret; for example, for the bimodal feature of LSMs and VLSMs in the pre-multiplied spectrum of streamwise fluctuations, the results of regular rough-bed OCF configured with uniform spheres in Cameron et al. [21] show a bimodal feature, while the results of low submergence and highly rough-bed OCF in the study by Ferraro et al. [28] showed no bimodal features.

This study aims to fill the gaps in research on irregularly arranged rough-bed OCF and provide a better understanding of VLSMs in OCF, with an emphasis on the less understood flow scenario of irregularly arranged rough-bed OCF. This study demonstrates the characteristics and presence of LSMs and VLSMs in irregularly arranged rough-bed OCF through velocity statistics and power spectrum analysis, and an analysis of the relationship between the peak wavelength of VLSMs and the aspect ratio (B/H). The remainder of this paper is organized as follows: Section 2 describes the experimental facilities and analysis methods. Section 3 presents the accuracy verification of the current measurements by statistical quantities and then shows the presence and characteristics of VLSMs based on spectral analysis. Finally, Section 4 summarizes the principal findings of this study.

2. Methodology

In this study, the streamwise, wall-normal, and spanwise directions were represented by x , y , and z , respectively. The instantaneous velocities in the corresponding directions are represented by u , v , and w , with the corresponding time-averaged velocities indicated by U , V , and W , respectively, and fluctuating velocities indicated by u' , v' , and w' , respectively. All

physical quantities normalized by friction velocity and kinematic viscosity are represented with a superscript “+”. The ensemble average is expressed as an overbar.

2.1. Facilities and Experiments

The experiments were carried out in a self-recirculating open-channel flume with a length of 28 m, a width of 0.56 m, and a height of 0.7 m at Chongqing Jiaotong University (as schematically depicted in Figure 1a). The channel bottom and sidewalls are composed of glass to facilitate the application of particle image velocity (PIV) measurements. The bed slope of the flume is adjustable, and the slope adjustment range is $-0.1\text{--}0.7\%$.

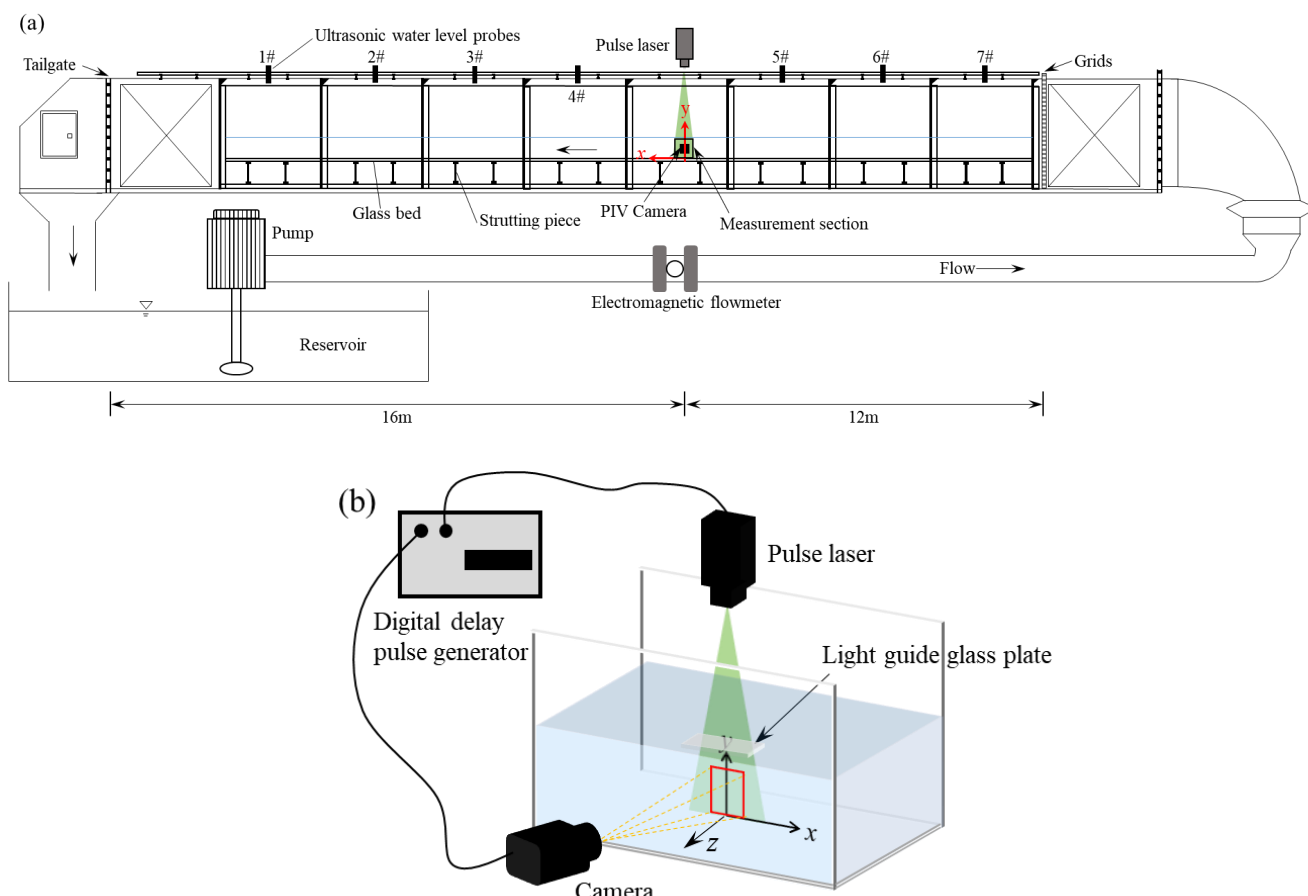


Figure 1. (a) Schematic of an open-channel flume (not to scale) and (b) PIV system arrangement (a small light guided glass plate (10 cm long, 5 cm wide and 0.2 cm thick) is arranged right above the water surface to eliminate the surface fluctuations).

Three rectifying grids with square holes of 25 cm^2 were placed at the flume entrance to flatten the flow and eliminate the potential large-scale fluctuations generated by the circulating system. Seven ultrasonic water-level gauges were arranged along the flume to monitor the water depth.

The measurement section was located 12 m downstream of the flume inlet. The slope of the flume was maintained at 2.5% for all flow cases. Three flow cases with different water depths were considered. The corresponding friction Reynolds number range was from 1800 to 4200 and was sufficiently high and large for the study of VLSMs. Further details regarding the flow condition parameters are presented in Table 1.

Table 1. Flow conditions for each flow case ^(a).

Case	<i>H</i> (m)	<i>B/H</i>	<i>u</i> (m^2/s)	<i>U_m</i> (m/s)	<i>u*</i> (m/s)	<i>F_r</i>	<i>Re</i>	<i>Re_t</i>	<i>k_s</i> ⁺
H055Re _t 1780	0.055	10.2	1.03×10^{-6}	0.428	0.034	0.583	22,757	1785	442
H075Re _t 2760	0.075	7.5	1.03×10^{-6}	0.506	0.038	0.590	36,714	2762	494
H100Re _t 4110	0.100	5.6	1.03×10^{-6}	0.586	0.042	0.592	56,671	4110	546

Notes: ^(a) *H*: water depth; *B/H*: width-depth ratio; *v*: kinematic viscosity; *U_m*: depth mean velocity; *u**: friction velocity, determined based on the log law with the von Kármán constant *k* = 0.412 and additive constant *A* = 5.26; *F_r*, Froude number; *Re* = *U_mH/v*, Reynolds number; *Re_t* = *u*H/v*, friction Reynolds number; *k_s*⁺ = *k_su*/v*, dimensionless roughness height.

A two-dimensional, high-frequency, high-precision PIV measurement system placed on a movable measurement frame above the flume was used to measure the instantaneous flow velocity.

The hardware of the PIV measurement system was composed of a high-speed CMOS camera (NX5-S2(Integrated Device Technology., California, America), 2560 × 1920 pixels), an 8 W semiconductor pulse laser, and a digital delay pulse generator. The laser wavelength was 532 nm, the sheet thickness was approximately 1 mm, and the single-pulse energy was 500 mJ. The maximum sampling rate of the PIV measurement system can reach 5000 Hz. Hollow glass spheres with a density of 1.03 g/mm³ and a median particle size of 10 mm were used as the tracer particles.

In each flow case, PIV measurements were performed at a sufficiently high frequency of 800 Hz to completely resolve small-scale coherent structures. The total sampling time duration *T* was sufficiently long, during which the main flow moved a distance along the streamwise direction *TU_m* up to over 10,000 water depths *h*, to obtain convergent spectral results of VLSMs.

For all cases, the obtained particle images were post-processed using the PIV software with multipass and multigrid window deformation algorithms. The initial and final integration window sizes were 64 × 64 and 16 × 16 pixels, respectively, with an overlap of 50% applied along both the streamwise and wall-normal directions. The resultant inner-scale normalized vector spacing ranged from 4 to 12. Additional PIV parameters are listed in Table 2.

Table 2. PIV parameters for each flow case ^(a).

Case	Image Size (Pixels)	Resolution (Pixel/mm)	<i>F_s</i>	<i>T</i> (s)	Number of Images	Δx^+	<i>TU_m/h</i>	$\Delta TU_m/h$	ΔT^+	<i>y*</i> (mm)
H055Re _t 1780	1024 × 128	0.062	800	1879.25	1503,400	4.22	14,616	0.0097	1.24	0.0323
H075Re _t 2760	1496 × 128	0.062	800	1544.51	1235,610	7.52	10,422	0.0084	1.81	0.0267
H100Re _t 4110	1600 × 128	0.062	800	1684.99	1347,990	11.99	9872	0.0073	2.46	0.0229

Notes: ^(a) *F_s*, sampling frequency of the velocity fields; *T*, total image acquisition time; Δx^+ , inner-scaled vector spacing in the streamwise direction; ΔT^+ , time interval between successive velocity fields; *y** = *v/u**, the viscous length scales.

2.2. Power Spectrum

The power spectrum is used to analyze the spectral characteristics of coherent structures. Because the measured data were discrete signals, the windowed discrete Fourier transform was used to calculate the velocity power spectrum.

$$E_i(f_x) = \sum_{n=0}^{N-1} u'_i(n)W(n) \exp\left[\left(\frac{-j2\pi}{N}\right)xn\right] \quad (1)$$

where *u'_i* is the fluctuating velocity, *i* = 1 and 2 represents the streamwise and wall-normal fluctuating velocity components, respectively, *j* is plural, *f_x* is the frequency component,

where $x = 0, 1, \dots, N - 1$, and W is the window function (in the present study, the Hamming window function was adopted). The power spectrum can be obtained as

$$S_{ij}(f_x) = \frac{1}{NM} \left| \left[E_i(f_x) E_j^*(f_x) \right] \right| \quad (2)$$

where $M = \frac{1}{N} \sum_{n=0}^{N-1} W^2(n)$ denotes the normalization of the window function. Based on Taylor's frozen flow assumption and the convection velocity, the frequency-based power spectrum can be converted into the wavenumber spectrum as follows:

$$S_{ij}(k_x) = \frac{u(y)}{2\pi} S_{ij}(f_x) \quad (3)$$

$$k_x = \frac{2\pi f_x}{u(y)} = \frac{2\pi}{\lambda_x} \quad (4)$$

where k_x is the wavenumber and λ_x is the wavelength. Following the literature, the time-averaged streamwise velocity $u(y)$ was used as the convection velocity. Although the obtained spectrum can be distorted in the long wavelength range, especially in the near-wall region, due to the application of Taylor's frozen flow hypothesis, this is still the most widely used method for obtaining the spatial spectrum for experimental studies. To facilitate comparisons with the results documented in the literature, a spectrum transformation based on Taylor's frozen flow hypothesis was used.

Based on the power spectrum, the contributions of different scale structures to the turbulent kinetic energy or Reynolds shear stress can be quantified based on the cumulative contribution fraction. For example, the cumulative contribution fraction to $\bar{u}_i \bar{u}_j$ from all scales smaller than the wavelength λ_x , denoted as γ_{ij} herein, can be obtained as

$$\gamma_{ij}(\lambda_x) = \frac{\int_0^{2\pi/\lambda_x} S_{ij}(\tilde{k}_x) d\tilde{k}_x}{\int_0^\infty S_{ij}(\tilde{k}_x) d\tilde{k}_x} \quad (5)$$

and $1 - \gamma_{ij}$ quantifies the contribution from all scales greater than λ_x .

3. Results and Discussion

3.1. Determination of the Theoretical Zero Point of Irregularly Arranged Rough-Bed

The theoretical zero point is an important parameter that must be predetermined for rough-bed turbulence research. However, it is difficult to accurately determine the theoretical zero point, particularly when the bed configuration is complex, owing to the complexity and variety of rough-wall configurations. Although many methods have been proposed in the literature, most are empirical, and the results obtained from different methods exhibit significant deviations. In this section, a more direct method is proposed to obtain a better estimation of the theoretical zero-point.

The new direct method is based on direct measurements of the rough-bed height, which are mainly realized by the high-precision structure from motion (SFM) technology [36]. The details of the method are explained herein by taking the rough-bed configurations used in this study as examples.

In this study, the rough-bed was configured with pebbles (median size $d_{50} = 1.5$ cm), and the rough-bed thickness was approximately $4d_{50}$ (Figure 2a). Figure 2b shows the reconstruction results of the bed topography and provides a preliminary demonstration of the random distribution feature of the rough-bed; where the gray pattern in the lower left corner of the figure is a cubic concrete block ($7 \times 7 \times 7$ cm 3) used for calibrating the rough-bed height.

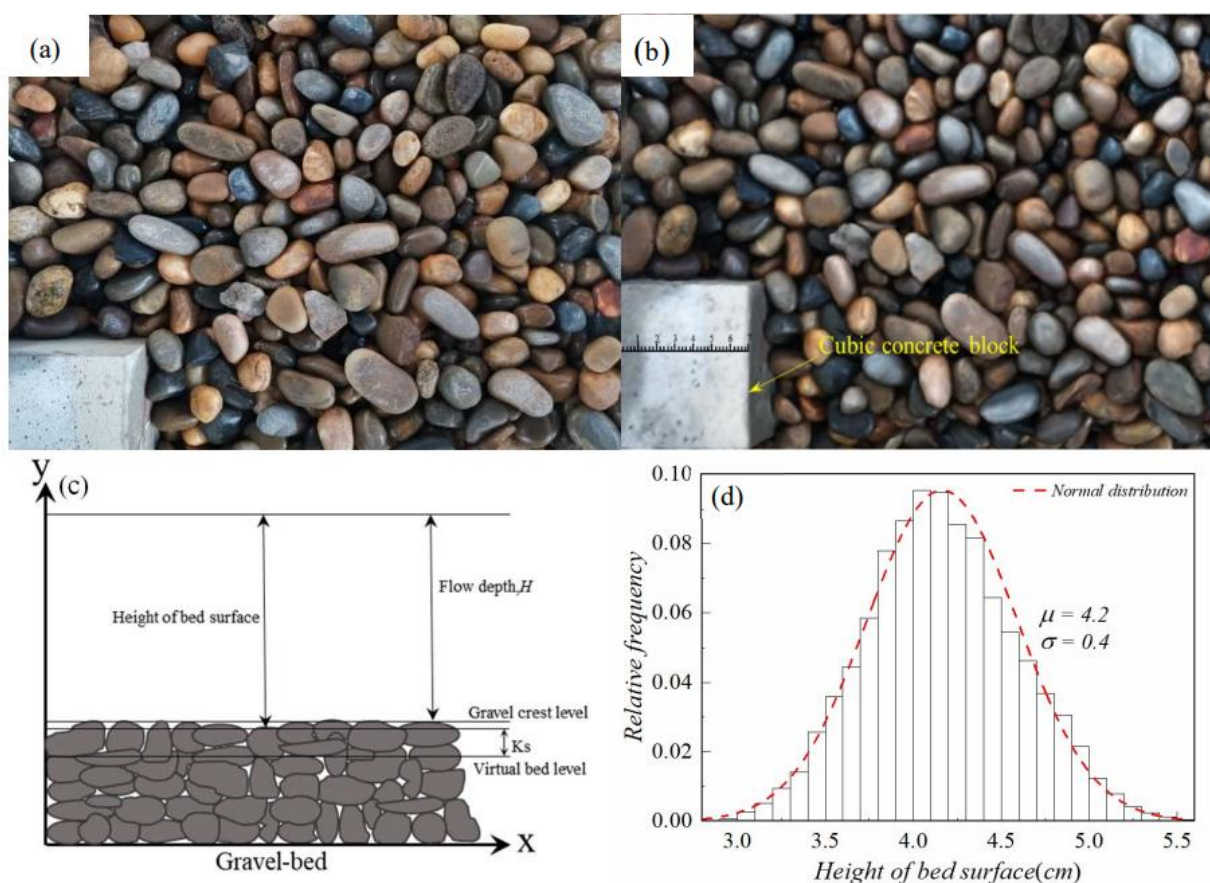


Figure 2. Characteristics of the rough-bed: (a) realistic view of the rough-bed surface ($18 \times 15 \text{ cm}^2$); (b) rough-bed terrain reconstructed by structure from motion (SFM) technology; (c) schematic of the height of the rough-bed surface; (d) probability distribution of bed surface height.

A large number of topographic photos of the bed surface were acquired (4000×3000 pixels and a focal length of 5 mm; over 1000 images were captured at each bed region of interest) by a movable camera to obtain accurate reconstruction results of the SFM. The camera was placed on a moving frame such that it could comprehensively move to change the imaging region, and the camera height was always kept constant. Dense and irregularly spaced interval photography ensures that the overlap rate between the two photos exceeds 60%. The real three-dimensional bed terrain was obtained by integrating topographic photos with the Agisoft PhotoScan software (<https://www.agisoft.com/>, version: 1.4.5.7354, accessed on 18 November 2022), with a reconstruction error within $\pm 0.6 \text{ mm}$ [37].

Based on the reconstructed three-dimensional bed terrain, the bed surface height at each pointwise position can be obtained based on the relative coordinates shown in Figure 2c. The lowest point of the riverbed surface height was considered the virtual bed level. Figure 2d shows a statistical histogram of the obtained bed surface height. The height distribution is observed to be symmetrical and to have a normal distribution. This is consistent with the observations of Nikora et al. [38], who found that gravel bed elevation can be considered to have an approximate normal distribution. For the rough-bed configurations, the mean bed height was 4.2 cm with a standard deviation of 0.4 cm.

The average distance between the elevation of the lower accessible point and the maximum roughness crest level was calculated and taken as the equivalent roughness height. The calculated roughness height was 1.3 cm, which is equivalent to the median particle size of the pebble. A direct measurement of the peak-to-valley height of the roughness elements was obtained (1.8 cm) based on the detailed 3D reconstruction information of the SFM.

3.2. Profiles of Typical Statistics

A preliminary investigation of the turbulent characteristics was performed. Profiles of typical statistics, including the time-averaged velocity, Reynolds shear stress, and turbulent intensity, obtained for data verification are presented in this section.

The time-averaged velocity profiles are shown in Figure 3a. Two profiles at positions corresponding to the pebble top and pebble gap are presented to reveal the potential measurement position effects on the resulting profiles. With an increase in the water depth, the velocity continuously increases and reaches a maximum at the free water surface. The maximum velocities under the three flow cases were approximately 0.36, 0.47, and 0.58 m/s, respectively. At the same time, the second-order polynomial fitting curve and 95% confidence interval are added to the velocity distribution data. According to the confidence level, the velocity near the bed surface has a certain deviation, but the flow velocity in other areas has a high degree of reliability. It shows that the experimental results in this paper are reliable. Figure 3b shows the normalized velocity profiles, with the velocity normalized with the friction velocity and the wall-normal position normalized with the equivalent rough height. Based on Figure 3b, within the wall-normal range of $0.5k_s$ – $4k_s$, the velocity profile is consistent with the rough-wall logarithmic law proposed by Dong [39]. Comparisons between the profiles at the pebble gap and top (Figure 3a) demonstrate that measurement locations have an impact on the time-averaged velocity profiles, and the impact is stronger in the near-water surface region than in the near-bed region. However, it is also worth noting that the difference between the two profiles is not significant, which can be more clearly observed in the normalized velocity profiles in Figure 3b. Based on these observations, the results obtained at the pebble gap were analyzed. The results obtained at the pebble top are no longer presented for brevity.

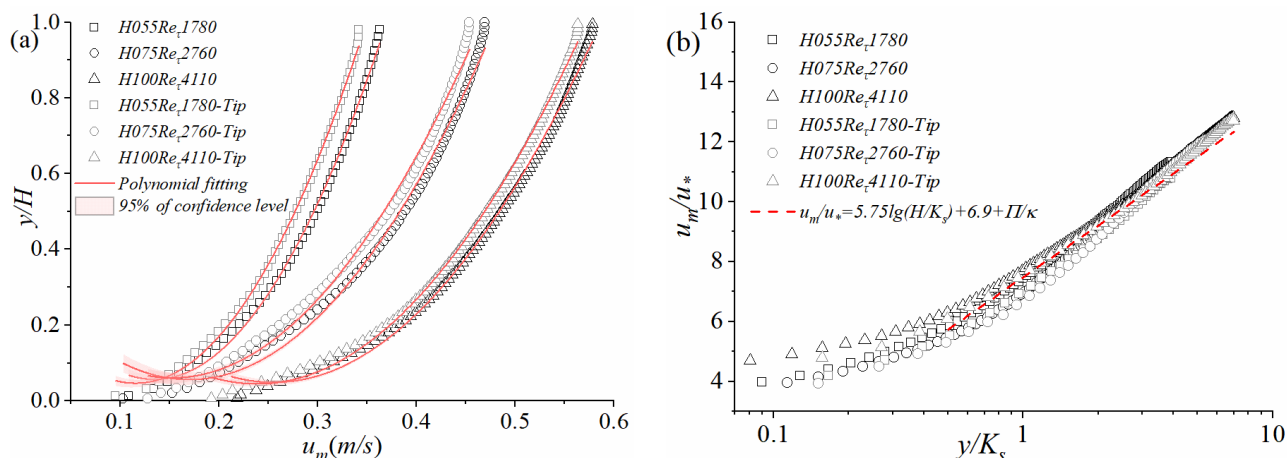


Figure 3. Time-averaged velocity profiles at different flow cases (Tip indicates that the starting point of the measurement is at the top of the pebble particles): (a) the time-averaged absolute velocity profiles; (b) the normalized velocity profiles processed by the friction velocity.

Figure 4a shows the profiles of Reynolds shear stress. It is clear that the normalized Reynolds shear stress is in good agreement with the theoretical linear line in the outer flow region. Under the $H100Re_t4110$ test condition, the dimensionless Reynolds shear stress per unit density attains a peak near $y/H = 0.1$ followed by a sharp decrease. The dimensionless Reynolds shear stress under $H055Re_t1780$ and $H075Re_t2760$ test conditions break over at $y/H = 0.2$. Compared with the other two groups of test conditions, $H100Re_t4110$ shows that the sudden change in the Reynolds shear stress is closer to the bed surface, indicating that the turbulent structure tends to develop toward the bed surface under the condition of a large water depth. This linear variation can be verified by the net-force (wall-normal gradient of the Reynolds shear stress) profile (Figure 4b). In Figure 4b, the net force is roughly constant at the outer region, indicating a linear variation of Reynolds shear stress

in the corresponding region. The variation of the wall-normal gradient of Reynolds shear stress near the bed surface is related to the aspect ratio (B/H). The wall-normal variation gradient of the viscosity effect under $H100Re_t4110$ is small due to the smaller aspect ratio, and the net force distribution presents a larger slope.

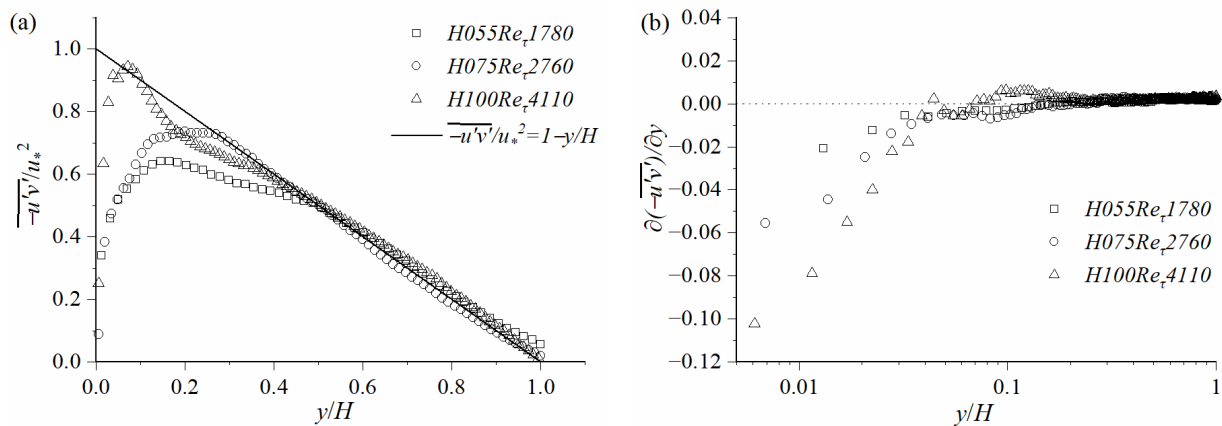


Figure 4. Wall-normal profiles of (a) the Reynolds shear stress and (b) the net force.

Finally, the profiles of turbulence intensity are discussed. The streamwise and wall-normal turbulence intensities are presented in Figure 5a and 5b, respectively. The turbulence intensity under the three experimental conditions exhibited the same varying regularity, but the magnitude was different. With increasing distance from the bed surface, the turbulence intensity continuously increased, and the increasing trend of the wall-normal turbulence intensity became more intense. Subsequently, the turbulence intensity in both directions decreased as the water depth increased. The empirical formula proposed by Nezu and Rodi [40] and the experimental data from Witz [41] for regular rough-bed OCF were included for comparison. The main trends of the present results are in agreement with the empirical formula and experimental data in the literature, with the only difference occurring in the turbulence intensity magnitude. In general, the results of the present study and the experimental results from Witz are slightly higher than those of the empirical formula because the Reynolds number is higher. The turbulence intensity of the present study was slightly larger than that of Witz's results because of the smaller roughness coefficient for the present rough-bed. Simultaneously, the friction Reynolds number and the roughness coefficient have a certain modulation effect on the streamwise and wall-normal velocity pulsations.

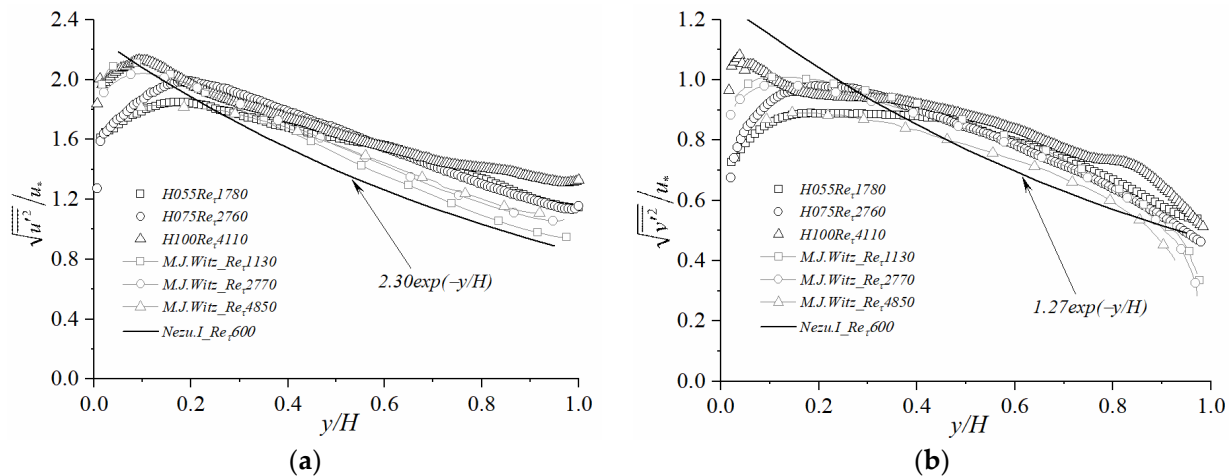


Figure 5. Profiles of (a) streamwise and (b) wall-normal turbulence intensities.

3.3. Presence of LSMs and VLSMs and Their Scales

Following the approach in LSM and VLSM studies, pre-multiplied spectra of streamwise velocity fluctuations, $k_x S_{uu}$, are presented in Figure 6 to show the presence of LSMs and VLSMs and their corresponding scales (the two white dotted lines). It is worth mentioning here that, as described by Peruzzi [26], to reduce the influence of spectrum distortion in the near wall region resulting from the application of Taylor's frozen flow hypothesis, spectra in the near wall region of $y/H < 0.1$ only are obtained. These are not discussed in detail here. Given the fact that LSCS, including LSMs and VLSMs, scale in outer units, the coordinates of the wavelength and wall-normal position are expressed and normalized in the outer units.

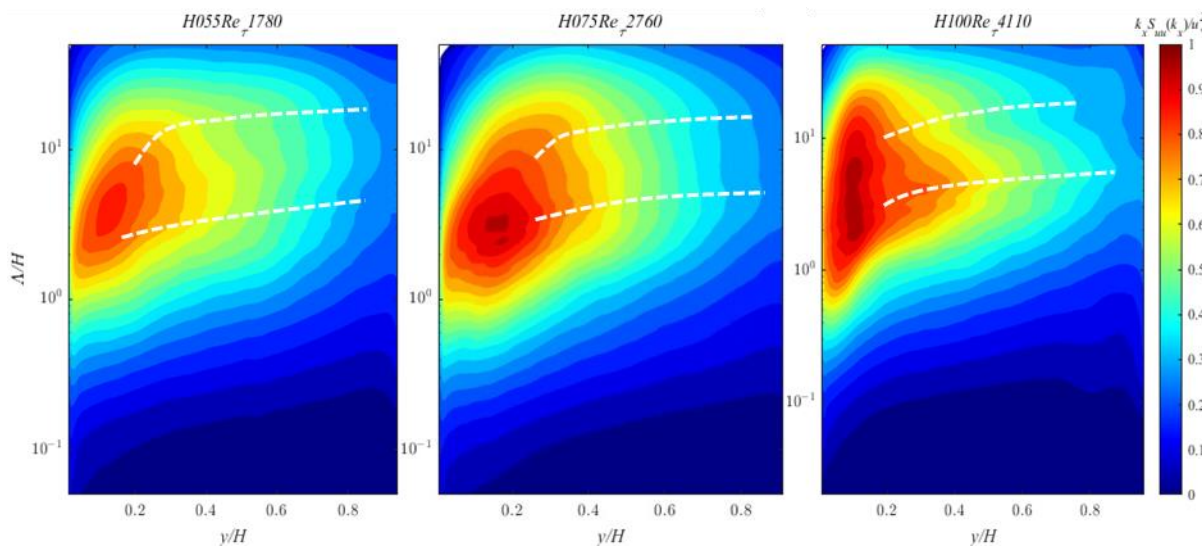


Figure 6. Pre-multiplied spectra of the streamwise velocity fluctuations.

Double peaks corresponding to LSMs and VLSMs can be clearly seen in the pre-multiplied spectrum of the streamwise velocity fluctuation shown in Figure 6. The double-peak phenomenon of LSMs and VLSMs in the present irregularly arranged rough-bed OCF is similar to that in the smooth-bed OCF [26] and the regular rough-bed OCF [21]. The spectral footprints of both the LSMs and VLSMs under the three conditions extend beyond $y/H = 0.8$, which is a unique characteristic of OCF. The existence of a VLSMs peak in the pre-multiplied spectrum also meets the requirement of the standard wall flow friction Reynolds number ($R_\tau > 1700$).

To visualize the scales of LSMs and VLSMs in more detail, the streamwise wavelengths corresponding to the peaks of the LSMs and VLSMs are identified and compiled in Figure 7. The results from the literature, including the empirical curve proposed by Monty et al. [42] based on experimental data for PF and CCF, the results of narrow smooth-bed OCF from Peruzzi et al. [26], and the results of regular rough-bed OCF from Cameron et al. [21], are also included for comparison.

Based on Figure 7, the wavelength of LSMs shows a slight increase along the wall-normal direction, and the results of different datasets are similar. However, for the wavelength of VLSMs, although the wall-normal trends of different datasets are also similar, the wavelength values differ from each other, even though the aspect ratio ranges of different datasets are similar. For example, although the aspect ratios of test 7 in Peruzzi et al. (corresponding to smooth-bed OCF), the H120 case in Cameron et al. (corresponding to regular rough-bed OCF), and H055Re_τ1780 in the present study (corresponding to irregularly arranged rough-bed OCF) are all approximately 10, the wavelengths of VLSMs in different scenarios exhibit the following trend: smooth-bed OCF > regular rough-bed OCF > irregularly arranged rough-bed OCF. This observation contrasts with Cameron et al.'s speculation that the wavelength of VLSMs exhibits a dependence on the aspect ratio, based

on which they proposed a linear relationship between the maximum wavelength of VLSMs along the wall-normal and aspect ratio. This conflict can be more clearly observed in Figure 8 and will be discussed later. Another interesting feature observed in Figure 7 is that the empirical curve obtained by Monty et al. roughly represents the upper envelope of the results of the present irregularly arranged rough-bed OCF.

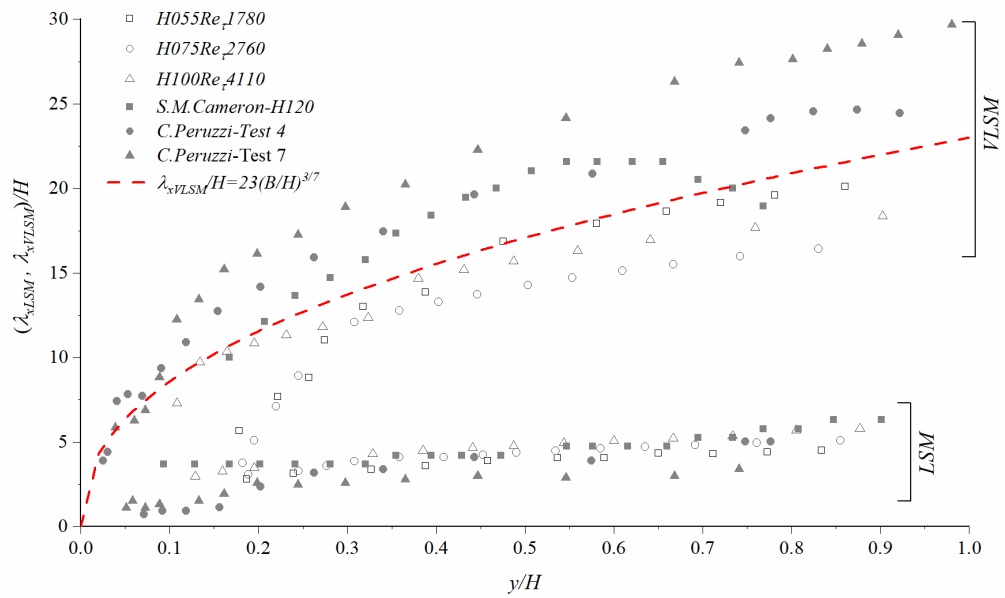


Figure 7. Wall-normal distributions of streamwise wavelengths corresponding to the peaks of LSMs and VLSMs.

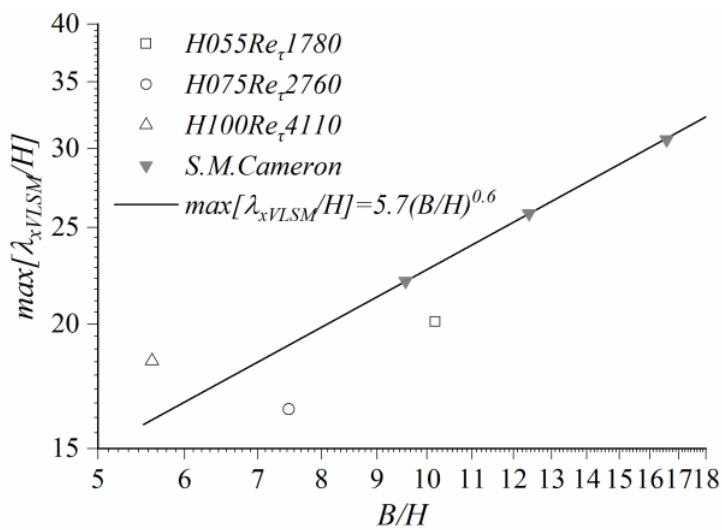


Figure 8. Maximum wavelength of VLSMs along the whole water depth versus flow aspect ratio.

To inspect the validity of Cameron et al. who proposed a relationship for the maximum wavelength of VLSMs along the whole water depth and flow aspect ratio, the results of the present irregularly arranged rough-bed OCF and those of Cameron et al. for a regular rough-bed OCF are depicted in Figure 8. Although the experimental data obtained by Cameron et al. for a regular rough-bed OCF satisfy well with the empirical relationship, the experimental data of the present study for the irregularly arranged rough-bed OCF exhibit deviations from the empirical curve. Considering this, the relationship proposed by Cameron et al. is not universal and must be revisited in the future.

3.4. Strength of VLSMs

After the presence and scales of LSMs and VLSMs have been determined, the strength of VLSMs (which can be quantified by their contributions to the turbulent kinetic energy and Reynolds shear stress) is further discussed in this subsection. It is worth mentioning that the strength of LSMs is not discussed since the consensus scale range of LSMs is still lacking; thus, the strength of LSMs has seldom been quantified in previous studies regarding LSMs and VLSMs. Furthermore, compared to LSMs, VLSMs play a major role in contributing to the turbulent kinetic energy and the Reynolds shear stress; therefore, the strength of VLSMs is more widely investigated in the literature [23], as well as in the present study.

Based on the spectra of streamwise velocity fluctuations S_{uu} and the cospectra of streamwise and wall-normal velocity fluctuations S_{uv} , cumulative contribution functions of γ_{uu} and γ_{uv} , which indicate the cumulative contribution fractions of different scale coherent structures to turbulent kinetic energy and Reynolds shear stress, are obtained. Figure 9 shows the γ_{uu} and γ_{uv} curves for the typical wall-normal positions. Figure 9 shows the scale range of VLSMs. Note that, following the widely used dividing scale in the literature, the streamwise wavelength of $\lambda_x = 3H$ was also adopted in the present study to divide LSMs and VLSMs (i.e., structures with $\lambda_x > 3H$ correspond to the scale range of VLSMs). Based on the γ_{uu} and γ_{uv} values at $\lambda_x = 3H$, that is, $\gamma_{uu}(\lambda_x = 3H)$ and $\gamma_{uv}(\lambda_x = 3H)$, the contribution of VLSMs to turbulent kinetic energy and Reynolds shear stress can be quantified by the values of $1 - \gamma_{uu}(\lambda_x = 3H)$ and $1 - \gamma_{uv}(\lambda_x = 3H)$, which are denoted as $g_{uuVLSMs}$ and $g_{uvVLSMs}$ for brevity, respectively. For the cumulative energy fraction of the streamwise velocity fluctuations, the Reynolds number and water depth changes are not considered, as shown in the figure. More than 65.8% of the energy contribution is from VLSMs, and more than 38.9% of the energy is contained in wavelengths longer than $10H$. Moreover, more than 47.5% of the Reynolds shear stress contribution is from VLSMs, and approximately 22–25% of the Reynolds shear stress is contained in wavelengths longer than $10H$.

The wall-normal profiles of $g_{uuVLSMs}$ and $g_{uvVLSMs}$ are shown in Figure 10. The contributions of VLSMs to turbulent kinetic energy in the irregularly arranged rough-bed OCF are greater than those in the smooth-bed OCF (gray solid sign). Another apparent discovery is that the contribution fraction of VLSMs to the turbulent kinetic energy shows a similar trend (i.e., increasing first in the inner region and then decreasing along with the water depth) for all three Reynolds number sections as well as that in smooth-bed OCF. Here, $g_{uvVLSMs}$ increase monotonically between $0 < y/H < 0.5$. At $y/H = 0.5$, $g_{uvVLSMs}$ reach approximately 0.5–0.6 and then gradually decrease. Similar to that of the smooth-bed OCF, VLSMs in the present irregularly arranged rough-bed OCF also play major roles in contributing to the turbulent energy and Reynolds shear stress. Comparisons between the results of the present irregularly arranged rough OCF and those of the smooth-bed OCF in the previous study by Duan et al. demonstrated that the contributions of VLSMs in the present irregularly arranged rough OCF are higher. As the turbulence intensity and Reynolds shear stress of the present irregularly arranged rough OCF are not lower than those of the smooth-bed OCF, the higher contributions of VLSMs to the turbulent kinetic energy and the Reynolds shear stress indicate that the VLSMs in the present irregularly arranged rough-bed OCF are stronger.

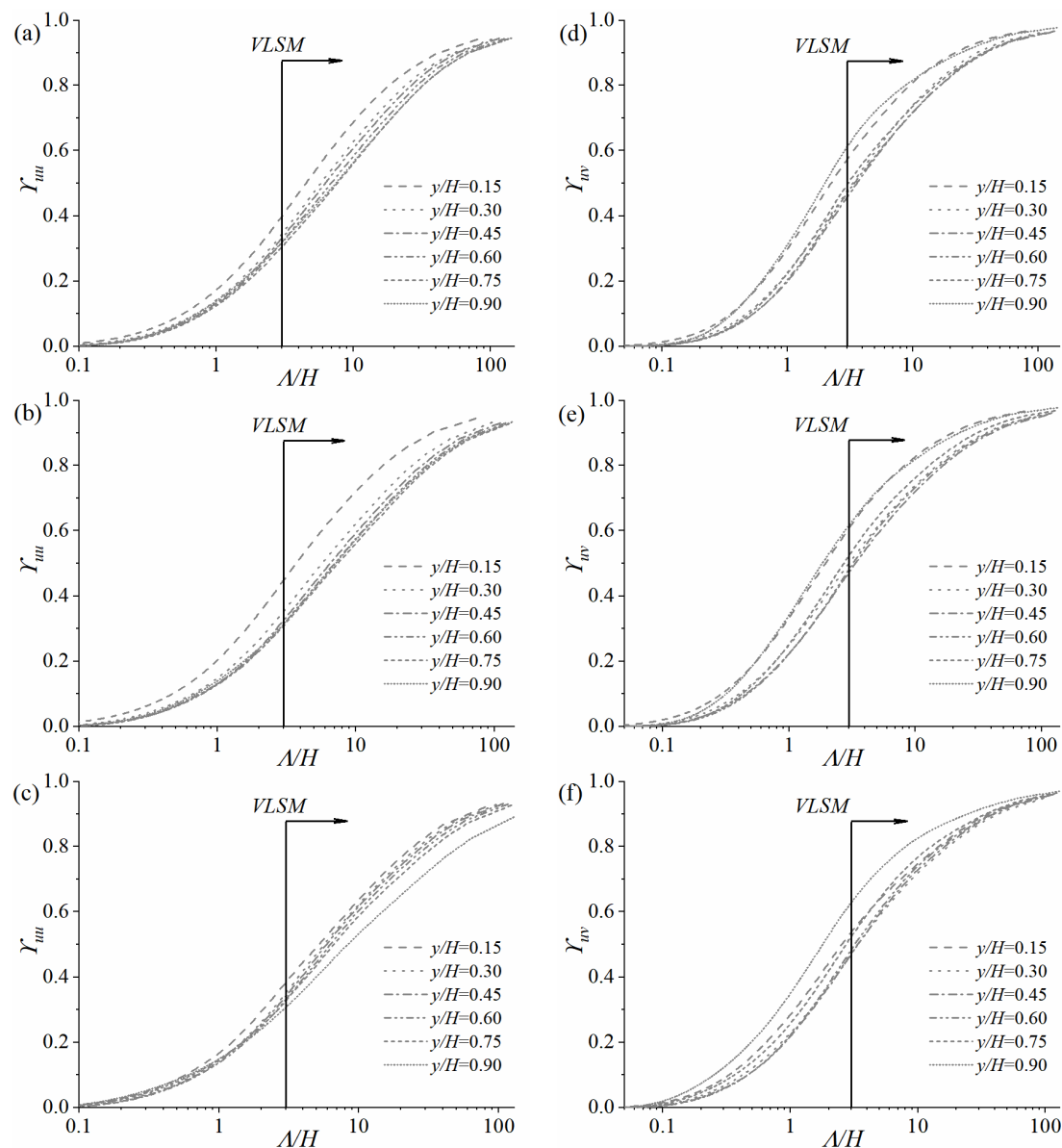


Figure 9. Cumulative contribution fractions of different scale structures to the streamwise kinetic energy (γ_{uu}) and Reynolds shear stress (γ_{ww}). (a,d) $H055Re_t1780$; (b,e) $H075Re_t2760$; (c,f) $H100Re_t4110$.

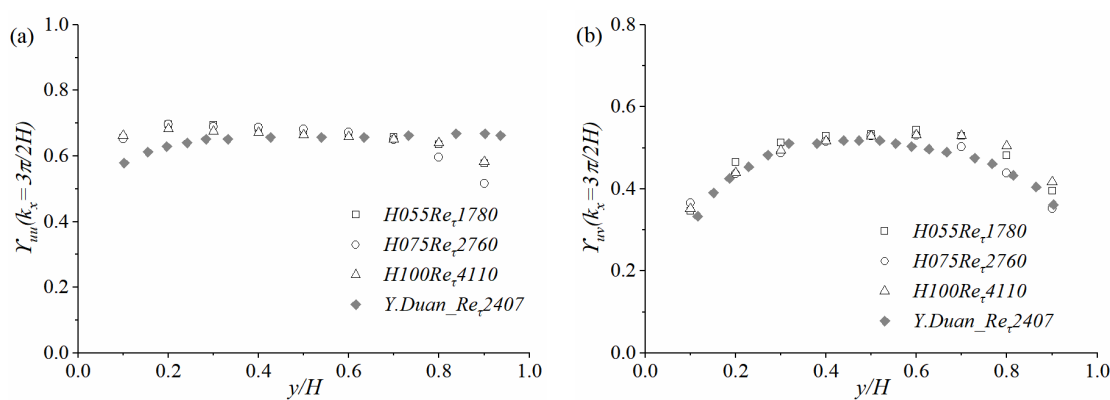


Figure 10. Wall-normal profiles of the contributions of VLSMs to (a) turbulent kinetic energy and (b) Reynolds shear stress.

4. Conclusions

High-frequency and long-duration PIV velocity measurements were performed under typical flow conditions (friction Reynolds numbers ranging from 1800 to 4200) on the irregularly arranged rough-bed OCF to demonstrate the presence and characteristics of VLSMs in an irregularly arranged rough-bed OCF. The aspect ratio of the flow ranges from 5.6 (low) to 10 (moderate), and the large submergence of the flow (ranging from 3.6 to 6.6) allows comparisons with the results of other bed forms in the literature. The main findings are summarized as follows:

- (1) The difference in the measurement locations (pebble gap and top) had a considerably small influence on the standardized time average velocity distribution. The typical statistics of the irregularly arranged rough-bed OCF are consistent with previous classical research. The friction Reynolds number and roughness coefficient have a certain modulation effect on the radial and vertical velocity pulsations.
- (2) The double peak phenomenon of LSMs and VLSMs exists in the present irregularly arranged rough-bed OCF, which is similar to the results of the smooth-bed OCF and the regular rough-bed OCF. Under the same aspect ratio ranges, the wavelengths of VLSMs on the irregularly arranged rough-bed OCF appear minimal among different bed scenarios (i.e., smooth-bed OCF, regular rough-bed OCF, and irregularly arranged rough-bed OCF), and the result of the smooth-bed OCF is the opposite.
- (3) The contributions of VLSMs to the turbulent kinetic energy and the Reynolds shear stress in the irregularly arranged rough-bed OCF are greater than those in the smooth-bed OCF. More than 60% of the turbulent kinetic energy and 40% of the Reynolds shear stress originate from VLSMs in the present irregularly arranged rough-bed OCF. Similar to those in the smooth-bed OCF, VLSMs in the present, irregularly arranged rough-bed OCF also play major roles in contributing to the turbulent energy and Reynolds shear stress.

Author Contributions: Conceptualization, P.Z.; data curation, Y.W.; formal analysis, Y.W.; funding acquisition, P.Z. and S.Y.; investigation, Y.W. and J.J.; methodology, Y.W. and R.Z.; writing—original draft, Y.W.; writing—review and editing, P.Z., C.H. and S.Y.; All authors have read and agreed to the published version of the manuscript.

Funding: This study was supported by the Science and Technology Research Program of Chongqing Municipal Education Commission (Grant No. KJQN202100731) and Chongqing Jiaotong University Graduate Scientific Research Innovation Project (“Experimental Study on Bed Load Deposition Characteristics of Decelerating Flow in Open Channels”, Municipal level, No. CYB21216).

Data Availability Statement: The data supporting the findings of this study are available from the corresponding author upon reasonable request.

Conflicts of Interest: The authors declare no conflict of interest.

References

1. Kim, K.C.; Adrian, R.J. Very large-scale motion in the outer layer. *Phys. Fluids* **1999**, *11*, 417–422. [[CrossRef](#)]
2. Brandt, L.; Coletti, F. Particle-laden turbulence: Progress and perspectives. *Annu. Rev. Fluid Mech.* **2022**, *54*, 159–189. [[CrossRef](#)]
3. Discetti, S.; Bellani, G.; Örlü, R.; Serpieri, J.; Sanmiguel Vila, C.; Raiola, M.; Zheng, X.; Mascotelli, L.; Talamelli, A.; Ianiro, A. Characterization of very-large-scale motions in high-Re pipe flows. *Exp. Therm. Fluid Sci.* **2019**, *104*, 1–8. [[CrossRef](#)]
4. Avila, M.; Barkley, D.; Hof, B. Transition to turbulence in pipe flow. *Annu. Rev. Fluid Mech.* **2023**, *55*, 575–602. [[CrossRef](#)]
5. Lee, J.H.; Sung, H.J.; Adrian, R.J. Space–time formation of very-large-scale motions in turbulent pipe flow. *J. Fluid Mech.* **2019**, *881*, 1010–1047. [[CrossRef](#)]
6. Bon, T.; Meyers, J. Stable channel flow with spanwise heterogeneous surface temperature. *J. Fluid Mech.* **2022**, *933*, A57. [[CrossRef](#)]
7. Camporeale, C.; Cannamela, F.; Canuto, C.; Manes, C. Stability analysis of open-channel flows with secondary currents. *J. Fluid Mech.* **2021**, *927*, A32. [[CrossRef](#)]
8. Hall, P. An instability mechanism for channel flows in the presence of wall roughness. *J. Fluid Mech.* **2020**, *899*, R2. [[CrossRef](#)]
9. Wu, X.; Wallace, J.M.; Hickey, J.-P. Boundary layer turbulence and freestream turbulence interface, turbulent spot and freestream turbulence interface, laminar boundary layer and freestream turbulence interface. *Phys. Fluids* **2019**, *31*, 045104. [[CrossRef](#)]

10. Li, D.; Luo, K.; Wang, Z.; Xiao, W.; Fan, J. Drag enhancement and turbulence attenuation by small solid particles in an unstably stratified turbulent boundary layer. *Phys. Fluids* **2019**, *31*, 063303.
11. Barros, J.M.; Christensen, K.T. Characteristics of large-scale and superstructure motions in a turbulent boundary layer overlying complex roughness. *J. Turbul.* **2019**, *20*, 147–173. [\[CrossRef\]](#)
12. Ren, H.; Laima, S.; Li, H. Numerical investigation of very-large-scale motions in a turbulent boundary layer for different roughness. *Energies* **2020**, *13*, 659. [\[CrossRef\]](#)
13. Bailey, S.C.C.; Canter, C.A.; Sama, M.P.; Houston, A.L.; Smith, S.W. Unmanned aerial vehicles reveal the impact of a total solar eclipse on the atmospheric surface layer. *Proc. R. Soc. A Math. Phys. Eng. Sci.* **2019**, *475*, 20190212. [\[CrossRef\]](#)
14. Efthimiou, G.C.; Kumar, P.; Giannissi, S.G.; Feiz, A.A.; Andronopoulos, S. Prediction of the wind speed probabilities in the atmospheric surface layer. *Renew. Energy* **2019**, *132*, 921–930. [\[CrossRef\]](#)
15. Gemmell, F. Investigating neutral and stable atmospheric surface layers using computational fluid dynamics. *Atmosphere* **2022**, *13*, 221. [\[CrossRef\]](#)
16. Alcántara-Ávila, F.; Hoyas, S. Direct numerical simulation of thermal channel flow for medium–high Prandtl numbers up to $Re_\tau = 2000$. *Int. J. Heat Mass Transf.* **2021**, *176*, 121412. [\[CrossRef\]](#)
17. Fytanidis, D.K.; García, M.H.; Fischer, P.F. Mean flow structure and velocity–bed shear stress maxima phase difference in smooth wall, transitionally turbulent oscillatory boundary layers: Direct numerical simulations. *J. Fluid Mech.* **2021**, *928*, A33. [\[CrossRef\]](#)
18. Zampiron, A.; Cameron, S.; Nikora, V. Momentum and energy transfer in open-channel flow over streamwise ridges. *J. Fluid Mech.* **2021**, *915*, A42. [\[CrossRef\]](#)
19. Deng, B.-Q.; Yang, Z.; Xuan, A.; Shen, L. Localizing effect of Langmuir circulations on small-scale turbulence in shallow water. *J. Fluid Mech.* **2020**, *893*, A6. [\[CrossRef\]](#)
20. Candelier, F.; Mehlig, B.; Magnaudet, J. Time-dependent lift and drag on a rigid body in a viscous steady linear flow. *J. Fluid Mech.* **2019**, *864*, 554–595. [\[CrossRef\]](#)
21. Cameron, S.M.; Nikora, V.I.; Stewart, M.T. Very-large-scale motions in rough-bed open-channel flow. *J. Fluid Mech.* **2017**, *814*, 416–429. [\[CrossRef\]](#)
22. Yao, J.; Chen, X.; Hussain, F. Direct numerical simulation of turbulent open channel flows at moderately high Reynolds numbers. *J. Fluid Mech.* **2022**, *953*, A19. [\[CrossRef\]](#)
23. Duan, Y.; Chen, Q.; Li, D.; Zhong, Q. Contributions of very large-scale motions to turbulence statistics in open channel flows. *J. Fluid Mech.* **2020**, *892*, A3. [\[CrossRef\]](#)
24. Duan, Y.; Zhong, Q.; Wang, G.; Zhang, P.; Li, D. Contributions of different scales of turbulent motions to the mean wall-shear stress in open channel flows at low-to-moderate Reynolds numbers. *J. Fluid Mech.* **2021**, *918*, A40. [\[CrossRef\]](#)
25. Zhang, P.; Duan, Y.; Li, D.; Hu, J.; Li, W.; Yang, S. Turbulence statistics and very-large-scale motions in decelerating open-channel flow. *Phys. Fluids* **2019**, *31*, 125106.
26. Peruzzi, C.; Poggi, D.; Ridolfi, L.; Manes, C. On the scaling of large-scale structures in smooth-bed turbulent open-channel flows. *J. Fluid Mech.* **2020**, *889*, A1. [\[CrossRef\]](#)
27. Wang, G.; Richter, D.H. Two mechanisms of modulation of very-large-scale motions by inertial particles in open channel flow. *J. Fluid Mech.* **2019**, *868*, 538–559. [\[CrossRef\]](#)
28. Ferraro, D.; Coscarella, F.; Gaudio, R. Scales of turbulence in open-channel flows with low relative submergence. *Phys. Fluids* **2019**, *31*, 125114. [\[CrossRef\]](#)
29. Cameron, S.M.; Nikora, V.I.; Witz, M.J. Entrainment of sediment particles by very large-scale motions. *J. Fluid Mech.* **2020**, *888*, A7. [\[CrossRef\]](#)
30. Diplas, P.; Dancey, C.L.; Celik, A.O.; Valyrakis, M.; Greer, K.; Akar, T. The Role of Impulse on the Initiation of Particle Movement Under Turbulent Flow Conditions. *Science* **2008**, *322*, 717–720. [\[CrossRef\]](#)
31. Valyrakis, M.; Diplas, P.; Dancey, C.L. Entrainment of coarse particles in turbulent flows: An energy approach. *J. Geophys. Res. Earth Surf.* **2013**, *118*, 42–53. [\[CrossRef\]](#)
32. Proust, S.; Berni, C.; Nikora, V.I. Shallow mixing layers over hydraulically smooth bottom in a tilted open channel. *J. Fluid Mech.* **2022**, *951*, A17. [\[CrossRef\]](#)
33. Richard, G.L.; Couderc, F.; Vila, J.P. Reconstruction of the 3-D fields with a depth-averaged model for open-channel flows in the smooth turbulent case. *J. Fluid Mech.* **2023**, *954*, A24. [\[CrossRef\]](#)
34. Ganju, S.; Bailey, S.C.C.; Brehm, C. Amplitude and wavelength scaling of sinusoidal roughness effects in turbulent channel flow at fixed $Re_\tau = 720$. *J. Fluid Mech.* **2022**, *937*, A22. [\[CrossRef\]](#)
35. Jelly, T.O.; Ramani, A.; Nugroho, B.; Hutchins, N.; Busse, A. Impact of spanwise effective slope upon rough-wall turbulent channel flow. *J. Fluid Mech.* **2022**, *951*, A1. [\[CrossRef\]](#)
36. Kovalenko, O.; Golyanik, V.; Malik, J.; Elhayek, A.; Stricker, D. Structure from articulated motion: Accurate and stable monocular 3D reconstruction without training data. *Sensors* **2019**, *19*, 4603. [\[CrossRef\]](#)
37. Lowe, D.G. Distinctive image features from scale-invariant keypoints. *Int. J. Comput. Vis.* **2004**, *60*, 91–110. [\[CrossRef\]](#)
38. Nikora, V.I.; Goring, D.G.; Biggs, B.J.F. On gravel-bed roughness characterization. *Water Resour. Res.* **1998**, *34*, 517–527. [\[CrossRef\]](#)
39. Wu, Z.; Singh, A.; Foufoula-Georgiou, E.; Guala, M.; Fu, X.; Wang, G. A velocity-variation-based formulation for bedload particle hops in rivers. *J. Fluid Mech.* **2021**, *912*, A33. [\[CrossRef\]](#)

40. Nezu, I.; Rodi, W. Open-channel flow measurements with a laser Doppler anemometer. *J. Hydraul. Eng.* **1986**, *112*, 335–355. [[CrossRef](#)]
41. Witz, M.J.; Cameron, S.; Nikora, V. Bed particle dynamics at entrainment. *J. Hydraul. Res.* **2019**, *57*, 464–474. [[CrossRef](#)]
42. Monty, J.P.; Hutchins, N.; Ng, H.C.H.; Marusic, I.; Chong, M.S. A comparison of turbulent pipe, channel and boundary layer flows. *J. Fluid Mech.* **2009**, *632*, 431–442. [[CrossRef](#)]

Disclaimer/Publisher’s Note: The statements, opinions and data contained in all publications are solely those of the individual author(s) and contributor(s) and not of MDPI and/or the editor(s). MDPI and/or the editor(s) disclaim responsibility for any injury to people or property resulting from any ideas, methods, instructions or products referred to in the content.